Molecular Dynamics of Iron Porphyrin-Catalyzed C−H Hydroxylation of Ethylbenzene

Yaling Zhang, Chaoqin Cao, Yuanbin She, Yun-Fang Yang,* and K. N. Houk*

Read Online

ACCESS | Metrics & More | Article Recommendations | Supporting Information

ABSTRACT: Quasi-classical molecular dynamics (MD) simulations were carried out to study the mechanism of iron porphyrin-catalyzed hydroxylation of ethylbenzene. The hydrogen atom abstraction from ethylbenzene by iron-oxo species is the rate-determining step, which generates the radical pair of iron-hydroxo species and the benzylic radical. In the subsequent radical rebound step, the iron-hydroxo species and benzylic radical recombine to form the hydroxylated product, which is barrierless on the doublet energy surface. In the gas-phase quasi-classical MD study on the doublet energy surface, 45% of the reactive trajectories lead directly to the hydroxylated product, and this increases to 56% in implicit solvent model simulations. The percentage of reactive trajectories leading to the separated radical pair is 98−100% on high-spin (quartet/sextet) energy surfaces. The low-spin state reactivity dominates in the hydroxylation of ethylbenzene, which is dynamically both concerted and stepwise, since the time gap between C−H bond cleavage and C−O bond formation ranges from 41 to 619 fs. By contrast, the high-spin state catalysis is an energetically stepwise process, which has a negligible contribution to the formation of hydroxylation products.
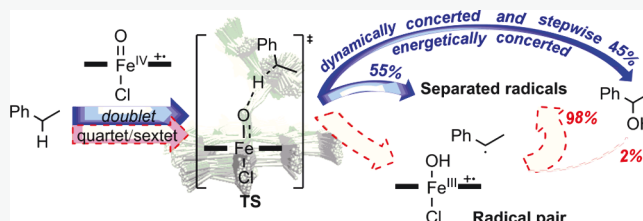
INTRODUCTION

Metalloporphyrin-catalyzed C−H bond hydroxylation has attracted significant attention as a biomimetic small molecule version of the cytochrome P450 enzyme-catalyzed hydroxylation.[1] The high valent iron-oxo ($Fe^{IV}=O$) porphyrin π-cation radical species (called Compound I) is generally accepted as the electrophilic oxidant in P450 enzyme-catalyzed hydroxylation reactions.[2] It was proposed that the metalloporphyrin-catalyzed C−H bond hydroxylation of ethylbenzene undergoes a hydrogen-atom-abstraction/oxygen-rebound (HAA/OR) mechanism,[3] which involves an ultrashort-lived radical pair of M−OH and benzylic radical (Scheme 1a). If the lifetime of the radical pair is too short to invert the stereocenter of the benzylic radical, the HAA step is the rate-determining and stereoselectivity-determining step in the case of the chiral metalloporphyrin catalyst applied. The OR step is typically barrierless. This HAA/OR mechanism is an intrinsically concerted pathway since no truly diffused radical pair intermediate exists. An early study by the McMahon group suggested that the P450 enzyme-catalyzed hydroxylation of $S(+)\alpha$-d-ethylbenzene exhibits a net conservation of the stereochemistry at the reacting carbon center.[4] Newcomb and collaborators conducted ultrafast "radical clock" experiments on the highly strained cyclic substrates with the cytochrome P450 enzymes and found that the measured radical lifetimes (80−200 fs) are too short to correspond to a fully free radical intermediate.[5]
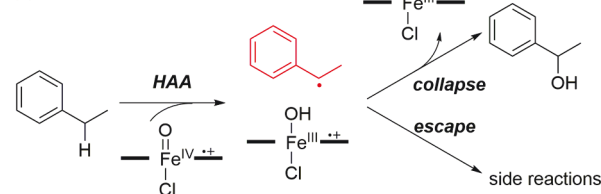
The free radical mechanism was also suggested in P450 enzyme-catalyzed hydroxylation of ethylbenzene (Scheme 1b

Scheme 1. (a, b) Possible Mechanisms of Fe-Porphyrin-Catalyzed Hydroxylation of Ethylbenzene
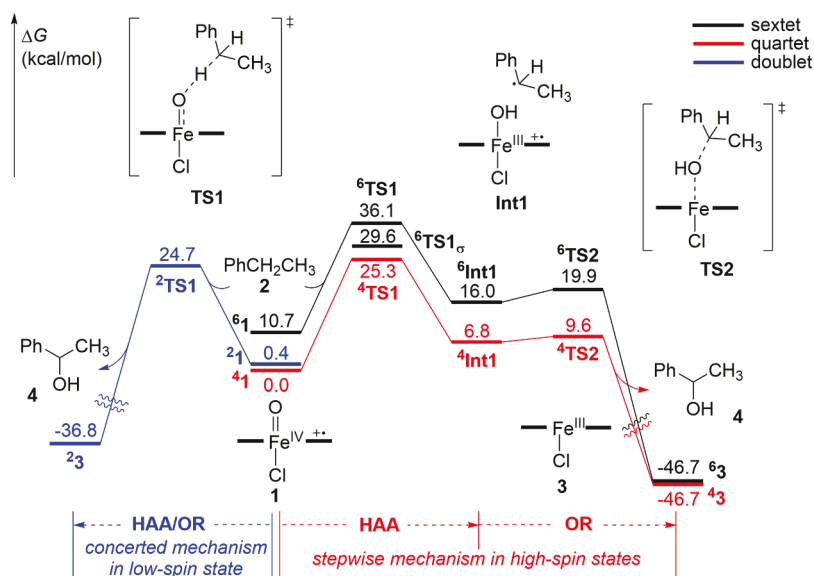
(a) **Hydrogen Atom Abstraction-Oxygen Rebound Mechanism**
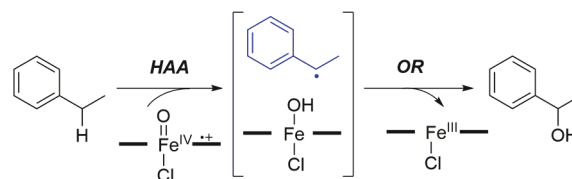
(b) **Free Radical Mechanism**

Figure 1. Free energy diagrams of ethylbenzene oxidation by the iron-oxo species in the gas phase. Gibbs free energy obtained at the (U)B3LYP/6-31G*-LANL2DZ level.

and Figures S1 and S2). White et al. observed that a considerable fraction (25−40%) of the ethylbenzene hydroxylation reaction involved a crossover of stereochemistry between the HAA and OR steps.[6] Groves and co-workers found that there is a significant loss of the original stereochemistry at the oxidized carbon center in the hydroxylation of norbornane.[7] The Groves group also proposed the "cage-escape" effect to address the chemoselectivity between oxygen and halogen rebounds in the reactions of HO−M(Por)−X species.[8]

Shaik and co-workers proposed the "two-state reactivity", which provides a mechanistic basis for metalloporphyrin-catalyzed hydroxylation reactions.[9] They found that the transition state for the rebound step lies 5 kcal/mol above the Fe−OH species on the high-spin quartet energy surface, and it is barrier-free for the low-spin doublet energy surface.[10] Yoshizawa and co-workers conducted classical trajectory calculations on alkane hydroxylation mediated by Compound I of cytochrome P450 and suggested that 200 fs is required for the rebound process under specific initial conditions, in which 0.1 kcal/mol kinetic energy is supplied to the HAA transition state along the reaction coordinate.[11] Recently, De Voss et al. studied the cytochrome P450-catalyzed rearrangement-free hydroxylation of methylcubane and proposed that the ultrafast radical rebound can be explained by a dynamically coupled C−H abstraction and C−O bond formation mechanism.[12] Chung and co-workers reported the effects of the iron (change in its coordination mode and spin state) on the dynamics of Fe-catalyzed hetero-Diels−Alder reaction.[13] Houk and co-workers have studied the molecular dynamics of dimethyldioxirane C−H oxidation, which also undergoes the HAA/OR mechanism.[14] They found that both OR and radical pair separation pathways can be observed, and the percentage of OR trajectories is higher in the implicit solvent than that in the gas phase. The lifetime of the radical pair ranges from 30 to 150 fs.

Previous studies of metalloporphyrin-catalyzed hydroxylation of alkanes and other hydrocarbons have led to different conclusions, especially on the nature of the radical pair and its impact on stereochemistry.[15] A concerted HAA/OR pathway

can rationalize the stereospecific/stereoselective hydroxylation of ethylbenzene. The existence of long-time free radical may lead to the inversion of stereochemistry.[16] It intrigued us whether the radical pair undergoes fast rebound to conserve the stereoselectivity or is able to reorient or even diffuse away.[17] To evaluate this, quasi-classical molecular dynamics (MD) simulations on a femtosecond time scale were carried out to study the dynamics of hydroxylation of ethylbenzene mediated by the iron-porphine model complex. While this manuscript was in preparation, Ess and Joy reported a quantum mechanics and molecular dynamics study of non-heme iron-oxo reactions with alkanes.[18] The results of our heme iron study are compared to this later in this manuscript.

■ COMPUTATIONAL METHODS

The density functional theory (DFT) calculations were carried out with the Gaussian 16 package.[19] Geometry optimization and energy calculations were performed with restricted B3LYP and unrestricted UB3LYP methods for closed shell and open shell species, respectively.[20] The LANL2DZ basis set[21] with ECP was used for the Fe atom, and the 6-31G* basis set[22] was used for other atoms. Frequency analysis was conducted at the same level of theory to verify the stationary points to be real minima or saddle points and to obtain the thermodynamic energy corrections. To ensure that the correct unrestricted wavefunctions were obtained, a stability test was carried out with the Gaussian keyword *stable = opt*. The single-point energies were calculated at the (U)B3LYP/6-31G*-LANL2DZ level using the SMD[23] solvation model (solvent = dichloromethane). Computed structures are illustrated using CYLview.[24]

Quasi-classical molecular dynamics simulations were performed at the level of (U)B3LYP/6-31G*−LANL2DZ by interfacing the Singleton's Progdyn code[25] with Gaussian 16. The initial configurations were generated by normal-mode sampling at 298.15 K from the optimized transition structure **TS1**. Along forward and backward directions, molecular configurations and velocities were propagated using the velocity Verlet algorithm with a time step of 1 fs. Thresholds for bond formations and trajectory terminations are listed in Table S1. Only productive trajectories without recrossing events were used for our analysis and discussion. The MD simulations, which require large amounts of CPU time, were performed on our lab's high performance computing (HPC) nodes. Generally, the simulation of one complete
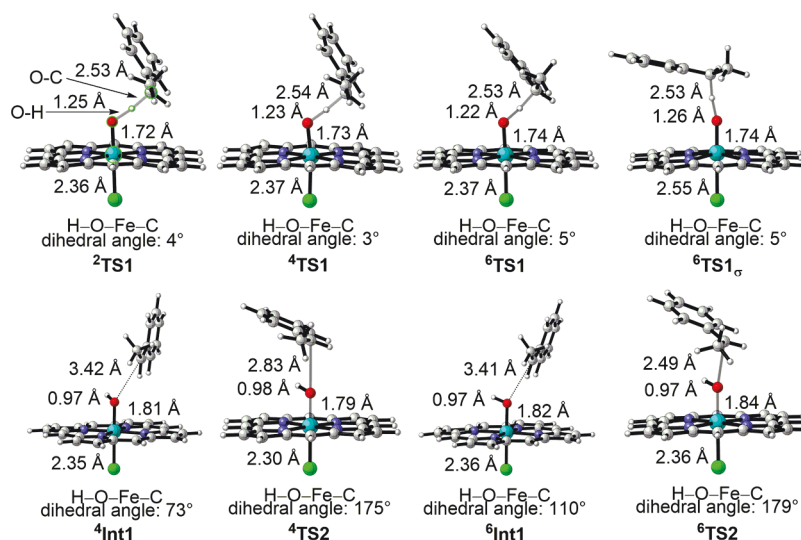
Figure 2. Optimized structures of the key transition states and intermediates of ethylbenzene oxidation by the iron-oxo species in the gas phase.
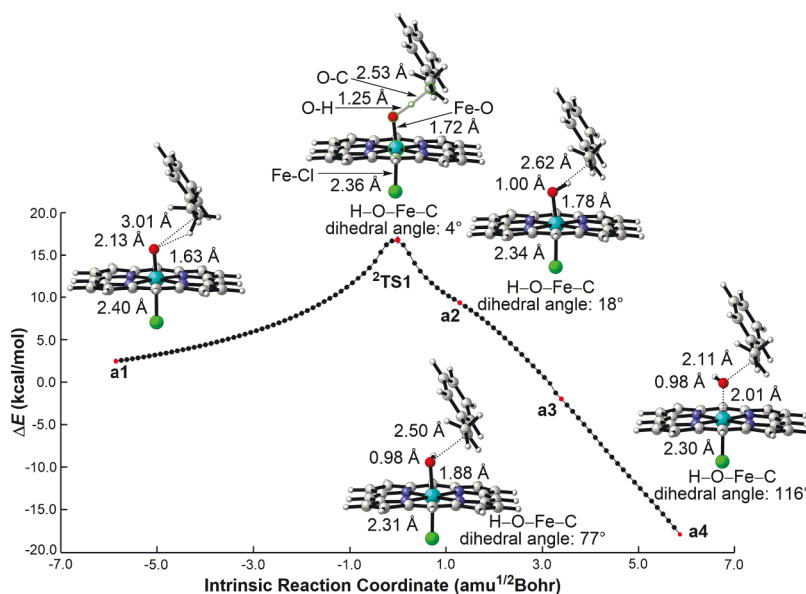

Figure 3. Intrinsic reaction coordinate (IRC) of ^{2}**TS1**.

MD trajectory for this system of 57 atoms required 2–6 days of CPU time (16 processors).

RESULTS AND DISCUSSION

DFT Mechanistic Study. The detailed description of the mechanism of iron porphyrin-catalyzed asymmetric hydroxylation of ethylbenzene was presented in our previous paper.[26] Here, we explored the key HAA/OR steps starting from the high valent iron-oxo species at the level of (U)B3LYP/6-31G*−LANL2DZ with Gaussian 16. Figure 1 shows the computed free energy diagram of ethylbenzene oxidation by the iron-oxo species in the gas phase. The corresponding free energy profile in the implicit solvent (DCM) (shown in Figure S3) is very similar to that in the gas phase. Figure 1 shows that ethylbenzene is hydroxylated by iron porphyrin in a "two-state reactivity" scenario.[27] In the HAA step, the low-spin (LS) transition state in the doublet state (^{2}**TS1**) is 24.7 kcal/mol. The high-spin (HS) transition state in the quartet state (^{4}**TS1**) is 25.3 kcal/mol, only 0.6 kcal/mol higher than ^{2}**TS1**. For both

doublet and quartet HAA transition states, ^{2}**TS1** and ^{4}**TS1**, only the π-attacking TS with the angle of Fe−O−H in ∼120° can be located. In contrast, for the sextet HAA transition states, both the π-attacking TS (^{6}**TS1**) with Fe−O−H in ∼120° and σ-attacking TS (^{6}**TS1**$_\sigma$) with Fe−O−H in ∼170° were located, which are 36.1 and 29.6 kcal/mol, respectively. The key transition structures and intermediates are shown graphically in Figure 2.

The LS rebound process in the doublet state is barrierless. To further confirm that the doublet pathway is a concerted process via the HAA/OR transition state ^{2}**TS1**, we have performed the intrinsic reaction coordinate (IRC) calculation on ^{2}**TS1** (Figure 3). Indeed, in the forward reaction from ^{2}**TS1**, the H-atom abstraction is closely followed by the C−O bond formation, and no diradical pair intermediate can be located. In ^{2}**TS1**, the H−O−Fe−C dihedral angle is 4°, and the abstracting H is located between O and the benzylic carbon center. This abstracting H moves away from the benzylic carbon along the reaction coordinate to facilitate the

C−O bond formation as the H−O−Fe−C dihedral angle changes from 18° in **a2** to 77° in **a3** and 116° in **a4**.

The HAA/OR process in LS is a concerted pathway with no diradical intermediate, and the rebound process has no barrier. On the contrary, there is a diradical intermediate in the HS energy profile, which has a barrier to rebound. In the HS process, the hydrogen atom abstraction by the iron-oxo complex leads to the benzylic radical and iron-hydroxo complex **Int1**. The benzylic radical and iron-hydroxo intermediate **Int1** can undergo a rebound step and produce the alcohol products. The oxygen rebound process via ^{4}**TS2** has a barrier of 2.8 kcal/mol measured from the diradical pair complex ^{4}**Int1**. Similarly, the oxygen rebound process via ^{6}**TS2** requires a barrier of 3.9 kcal/mol with respect to the diradical complex ^{6}**Int1**. The separated benzylic radical plus the Fe−OH species in singlet, triplet, and quintet states were calculated to be 0.9, 2.2, and 9.7 kcal/mol, respectively (Figure S4). The free energy diagram of ethylbenzene oxidation by the iron-oxo species measured from the separated benzylic radical plus the Fe−OH species in the implicit solvent (DCM) is shown in Figure S5.

The free radical intermediate may diffuse or reorient to rebound or undergo other radical reactions. To further deepen the understanding of the feature of the diradical intermediate, we have computed the energetics of a possible side reaction, in which the iron-hydroxo species further abstracts a β-hydrogen of the benzylic radical to form styrene and a Fe-aqua complex. On the doublet energy surface, this desaturation process has a free energy barrier of 10.3 kcal/mol in the gas phase (Figure S6) and 5.4 kcal/mol in the implicit solvent (Figure S7) with respect to the separate diradical intermediate, respectively. Therefore, the desaturation process is unfavorable compared with the oxygen rebound process.

Molecular Dynamics Study. The distribution of sampled transition state geometries with overlay visualization is shown in Figure S8. Figure 4 shows two typical trajectories from the
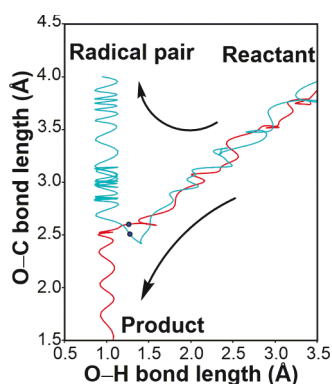
Figure 4. Two typical trajectories from reaction dynamics simulation. Blue dot marks are sampled TS points used to initiate trajectories.

reaction dynamics simulation of the hydroxylation of ethylbenzene in the gas phase represented by the O−H and O−C bond distances. The HAA/OR trajectory is shown in red, and the radical pair separation trajectory is shown in cyan. The snapshots of the two typical MD trajectories in the gas phase are also shown in Figure 5. The O−H and O−C bond lengths are labeled on the graphic. Both trajectories involve similar transition states with H transfer from the benzylic C−H bond to iron-oxo. At 0 fs, which corresponds to the transition state

structure, the starting point for the trajectories can result in mainly two destinations, the oxygen-rebound and the radical pair separation. The formed O−H bond lengths are 1.26 Å for the oxygen-rebound trajectory and 1.27 Å for the radical pair separation trajectory. The O−C bond lengths for the oxygen-rebound trajectory are 2.60 Å at 0 fs, 2.52 Å at 20 fs, and 1.44 Å at 57 fs. In the radical pair separation trajectory, the O−C distance increases from 2.51 Å at 0 fs to 2.88 Å at 59 fs and 4.00 Å at 193 fs. So, there is a clear separation of the benzylic radical and the iron-hydroxo species.

Figure 6 shows the time-resolved view of the change in the H−O−Fe−C dihedral angle, which was noted as the C−O−H angle in Ess and Joy's study,[18] in the HAA/OR trajectory via ^{2}**TS1** in the gas phase. In ^{2}**TS1**, the C−H−O angle is almost kept collinear for the H-atom abstraction process and the H−O−Fe−C dihedral angle is 4°. The H−O−Fe−C dihedral angle significantly changes over time for the O-rebound process, especially at 45 fs; there is a dramatic change in the H−O−Fe−C dihedral angle. This indicates that the rotation around the Fe−O bond is the major reaction coordinate in this O-rebound process.[18,28]

In addition, we also explored some changes in the bond distances along the trajectories. Figure 7 shows the time-resolved view of the changes in the bond distances for both the HAA/OR trajectory and the radical pair separation trajectory via ^{2}**TS1** in the gas phase. The O−H distance gradually decreases to around 1.00 Å over time, while the Fe−Cl and Fe−O distances remain almost constant in both HAA/OR and radical pair separation trajectories. The main difference between the two trajectories is that the O−C distance is shortened to 1.5 Å in the oxygen rebound trajectory, while the O−C distance is lengthened in the radical pair separation trajectory.

The distributions of the quasi-classical MD trajectories in the gas phase and implicit solvent (DCM) are summarized in Table 1 and Table S2. The number of oxygen rebound trajectories via ^{2}**TS1** is larger than that via ^{4}**TS1** and ^{6}**TS1**, whether in the gas phase or implicit solvent. This suggests that the energy surface on the doublet state is responsible for the formation of the hydroxylation product, although the energy difference between ^{2}**TS1** and ^{4}**TS1** is minimal ($\Delta\Delta G^{\ddagger}$ = 0.6 kcal/mol). Therefore, the reaction pathways via HS energy surfaces have a negligible contribution to the formation of the hydroxylation product. Meanwhile, the radical pair formation, which is detrimental to the stereoselectivity of hydroxylation reaction, results from both LS and HS energy surfaces.

The trajectories of the quasi-classical MD simulations of iron porphyrin-catalyzed hydroxylation of ethylbenzene on the doublet, quartet, and sextet potential energy surfaces are also shown in Figure 8. The trajectories via ^{2}**TS1** in the gas phase are displayed in Figure 8a. In gas-phase simulations, 45% of the reactive trajectories directly lead to the hydroxylation product, while in the implicit solvent (DCM), the percentage increases to 56% (Figure S9a). The trajectories via ^{4}**TS1** in the gas phase and implicit solvent (DCM) are displayed in Figure 8b and Figure S9b, respectively. Interestingly, in gas-phase simulation on ^{4}**TS1**, 98% of the reactive trajectories lead to the radical pair, and only 2% of the reactive trajectories directly lead to the hydroxylation product. Similarly, in implicit solvent model simulations, 100% of the reactive trajectories leads to the radical pair, and there are no oxygen rebound trajectories via ^{4}**TS1**. The trajectories via ^{6}**TS1** in the gas phase (Figure 8c) and implicit solvent (Figure S9c) are very similar. The quasi-
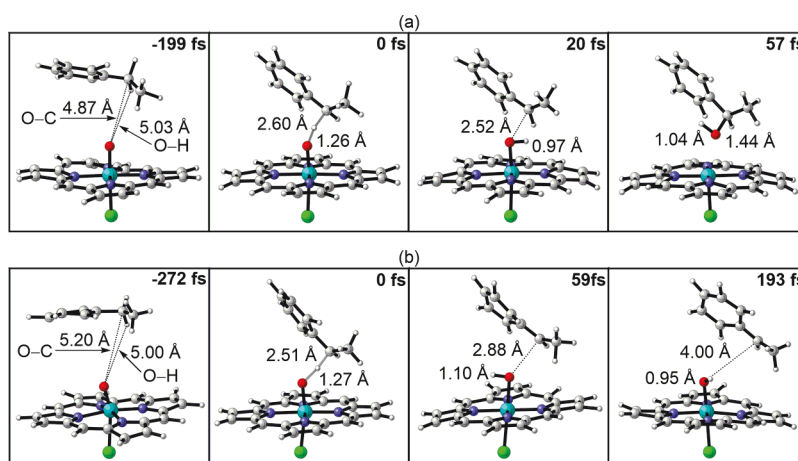
Figure 5. Snapshots of two typical reactive trajectories for the C−H bond hydroxylation of ethylbenzene by the iron-oxo species. (a) Oxygen-rebound trajectory, in which the hydroxylation of ethylbenzene gives 1-phenylethanol. (b) Radical pair separation trajectory, in which the benzylic radical and iron-hydroxo separate after HAA from ethylbenzene. The 0 fs panels correspond to the TS geometry where trajectories were initiated.
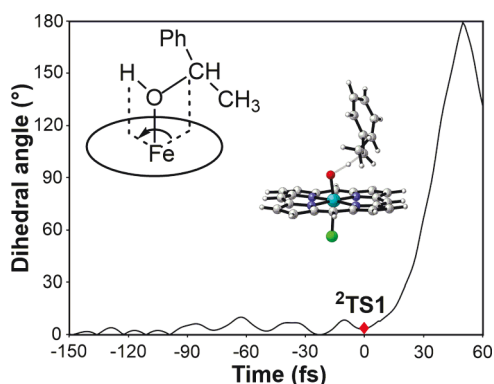
Figure 6. Change in the dihedral angle of H−O−Fe−C in HAA/OR via ^{2}TS1 in the gas phase. ^{2}TS1 is shown in red diamond.

classical MD simulations of iron porphyrin-catalyzed hydroxylation of ethylbenzene suggest that the HS energy surfaces are ineffective for the HAA/OR pathway.

Based on the above results, we analyzed the time gap in forming O−H and O−C bonds. The distribution of the time gap between the formation of O−H and O−C bonds in the oxygen rebound trajectories propagated on the doublet potential energy surfaces in the gas phase is shown in Figure 8d. The average time gap is 99 fs in the gas phase, while the

Table 1. Dynamics Results with Trajectories Initiated from TS1 in the Gas Phase

| transition structures	total trajectories	reactive trajectories	hydroxylation product (%)	radical pair (%)
^{2}TS1	570	394	45%	55%
^{4}TS1	306	270	2%	98%
^{6}TS1	345	301	2%	98%

average time gap increases to 156 fs in the implicit solvent (Figure S9d). The solvent can influence the average time gap of the oxygen rebound trajectories and increase the lifetime of the free radical intermediates.[29] Houk et al. defined 60 fs as the boundary between the dynamically concerted mechanism (the time gap of formation of two bonds $\tau \leq 60$ fs) and the dynamically stepwise mechanism (the time gap of formation of two bonds $\tau \geq 60$ fs).[30] This duality of mechanism is also exemplified in Figure 8e,f. Figure 8e shows the 46 fs time gap trajectory in which, after the formation of the O−H bond, the O−C bond oscillates around 2.5 Å for about one vibration period of the O−H bond and then decreases to 1.5 Å. This dynamical behavior indicates that no well-defined radical pair intermediate is generated along the trajectory, suggesting a dynamically concerted mechanism. Figure 8f displays the 229 fs time gap trajectory, in which the O−C distance increases to about 3.0 Å after the O−H bond is formed and vibrates
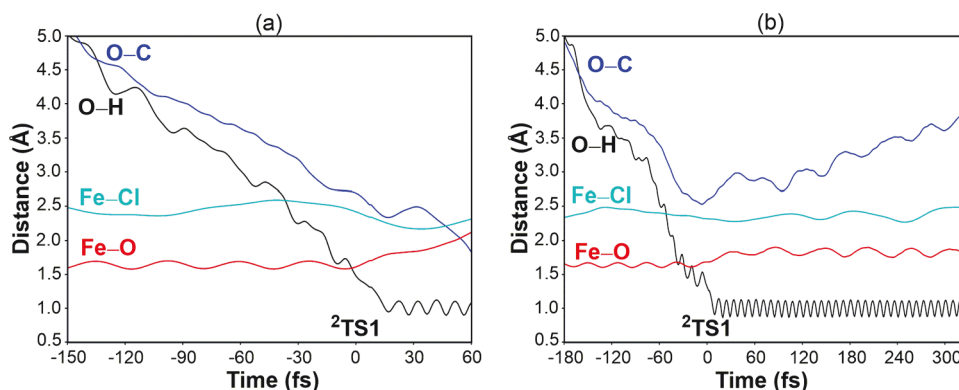
Figure 7. (a) Changes in bond distances in a HAA/OR trajectory via ^{2}TS1 in the gas phase. (b) Changes in bond distances in a radical pair separation trajectory via ^{2}TS1 in the gas phase.
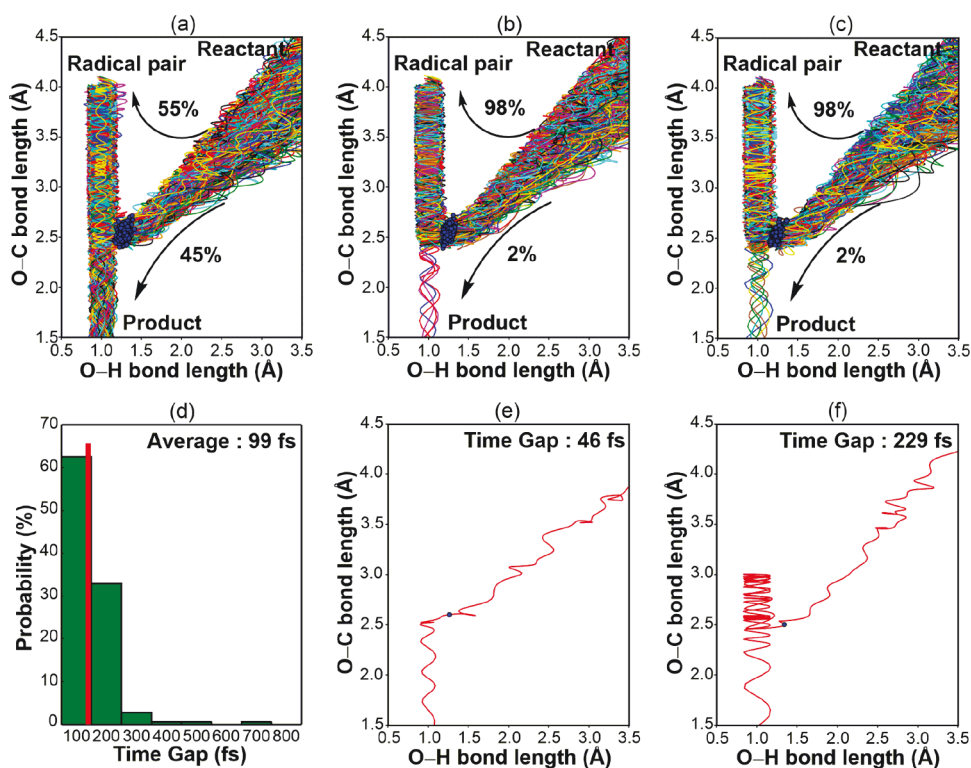
Figure 8. (a) Distribution of the reactive trajectories propagated via ^{2}TS1 in the gas phase. (b) Distribution of the reactive trajectories propagated via ^{4}TS1 in the gas phase. (c) Distribution of the reactive trajectories propagated via ^{6}TS1 in the gas phase. (d) Distribution of time gap between formation of the O−H and O−C bonds in the oxygen rebound trajectories propagated via ^{2}TS1 in the gas phase. (e) Oxygen-rebound trajectory with the 46 fs time gap. (f) Oxygen-rebound trajectory with the 229 fs time gap. Blue dot marks are sampled TS points used to initiate trajectories.
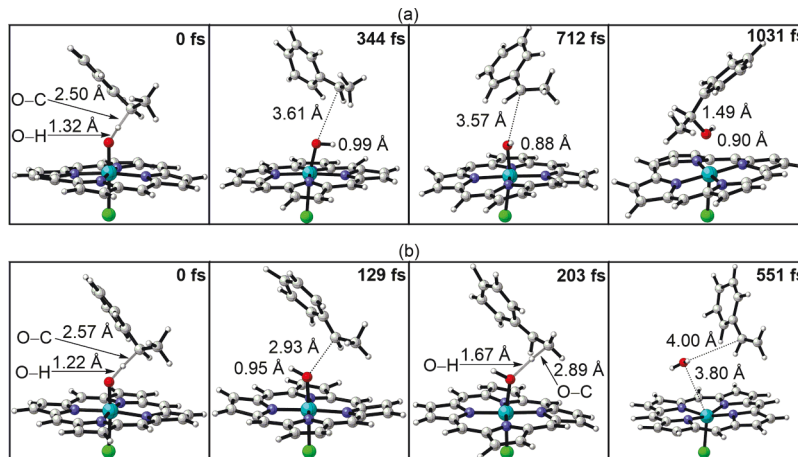
Figure 9. Snapshots of two kinds of radical pair trajectories. (a) Snapshot of a trajectory with an inverted configuration at benzylic carbon. (b) Snapshot of a trajectory involving β-hydrogen abstraction.

nearby. In all, this reaction is both concerted and stepwise dynamically.

In addition, we also found two other pathways in the radical pair trajectories. Figure 9 shows the snapshots of two kinds of radical pair trajectories: the snapshot of the pathway involving an inverted configuration at the benzylic radical and a β-hydrogen abstraction trajectory. In Figure 9a, the H-atom abstraction at *pro-R* forms the benzylic radical. There is an apparent flipping of the benzylic radical from 344 to 712 fs followed by generation of the hydroxylation product with *S*-configuration at 1031 fs, with an O−C bond length measuring 1.49 Å (also shown in Movie S1). The radical pair separation

trajectories were terminated if the O−C distance is >4.0 Å, and the simulation time is generally around 200 fs. Therefore, a longer time (>1000 fs) is needed for simulation of the formation of the product with an inverted configuration. Figure 9b shows the snapshots in the pathway of β-hydrogen abstraction by the iron-hydroxo species to form styrene. The iron-hydroxo species abstracts the β-hydrogen of the benzylic radical at 203 fs (Movie S2). Finally, the styrene will be formed, and the newly generated water molecule will dissociate from the aqua-Fe-porphyrin complex. We further examined all the separated radical pair trajectories and found that only a few such trajectories are generated in the dynamics simulations

(Tables S3 and S4). Although the benzylic radical may undergo rebound or desaturation reactions on a longer time scale, our MD simulations are appropriate to investigate ultrafast chemistry occurring within femtosecond to picosecond time scales. As such, many hydroxylated and/or desaturated products may not be observed due to this limited time window.

We investigated the impact of spin contamination on trajectory dynamics.[20a,31] The expected values for $\langle \hat{S}^2 \rangle$ are 0.75, 3.75, and 8.75 for pure doublet, quartet, and sextet states, respectively. Table S5 shows the range of $\langle \hat{S}^2 \rangle$ values in the regions of the initial sampled transition states, hydroxylation products, and radical pairs. The deviation of the exact value from the expected value is a useful diagnostic tool for assessing spin contamination in unrestricted wave functions.[31b] We found that the exact value for $\langle \hat{S}^2 \rangle$ ranges from 0.77 to 1.04 in the region of the initial sampled doublet transition states, indicating some level of spin contamination in the doublet state. The values of $\langle \hat{S}^2 \rangle$ as a function of time in all oxygen rebound trajectories via ^{2}TS1 in the gas phase are shown in Figure S10 and fall within the range of 0.77–1.01. The exact value for $\langle \hat{S}^2 \rangle$ in all radical pair separation trajectories via ^{2}TS1 in the gas phase ranges from 0.75 to 1.27, as illustrated in Figure S11. In contrast, there was minimal spin contamination in the initial sampled quartet and sextet transition states, with $\langle \hat{S}^2 \rangle$ values around 3.75 and 8.75, respectively. In all the radical pair separation pathways via ^{4}TS1 and ^{6}TS1, the exact values for $\langle \hat{S}^2 \rangle$ closely matched the corresponding expected values over time (Figures S12 and S13). However, along 55% of the radical pair separation pathways via ^{2}TS1, the exact values of $\langle \hat{S}^2 \rangle$ deviated from the ideal values due to significant contributions from unwanted spin states, ultimately leading to a $\langle \hat{S}^2 \rangle$ value of approximately 1.00. Therefore, we speculated that spin contamination facilitated dissociation, resulting in more radical pair separation pathways.

The high percentage of the radical pair separation trajectories, which is although overestimated due to the spin contamination, and the rotation of the benzylic radical are eroding the stereoselectivity. That is the cause of low enantioselectivity in many biomimetic metalloporphyrin-catalyzed hydroxylation of ethylbenzene.[32] By contrast, in P450 enzyme-catalyzed hydroxylation reactions, the high stereoselectivity is enforced by the tight-binding enzymatic environment.[33]

In the implicit solvent, the oxygen rebound trajectories and the time gaps are increased compared with those in the gas phase. So far, various studies have explained the influence of the "solvent cage" effect on the reaction trajectories.[30c,34] Houk and co-workers use a QM/MM model with direct dynamics simulations to support the water-accelerated Diels–Alder reaction,[30c] which was proposed by Jorgensen and co-workers that there is a preferential H-bond stabilization in the TS.[34e] In addition, Singleton and co-workers highlighted the role of the solvent dynamics in studying the nature of a betaine intermediate for a Witting reaction.[34a] To better understand the influence of the solvent effect on the metalloporphyrin-catalyzed hydroxylations of ethylbenzene, the molecular dynamics simulations with explicit solvent are currently being investigated in our laboratory.

As we mentioned in the Introduction, Ess and Joy reported a DFT-based quasi-classical direct dynamics study of non-heme iron-oxo reactions with alkanes.[18] Both heme and non-heme iron-oxo reactions involve competitive post-hydrogen atom transfer/abstraction reactions, such as radical rebound, dissociation, and desaturation reactions. In our DFT and dynamics studies of heme iron-oxo reactions with ethylbenzene, different spin states including doublet, quartet, and sextet states were all investigated. The HAA/OR process on the doublet energy surface is nonsynchronous concerted, which is consistent with the study of non-heme complex 4 by Ess and Joy. The nonsynchronous dynamically concerted process on doublet leads to fast rebound trajectories, which are facilitated by a dynamic matching between the rotational motion of the Fe−OH bond and the collision with the carbon radical. In addition, reactions with different spin states have different dynamic behaviors. In the gas phase study on the doublet energy surface, 45% of the MD reactive trajectories lead to the hydroxylated product, and 55% of the MD reactive trajectories lead to the radical pair separation/dissociation, which is likely exaggerated due to spin contamination that mixes in higher multiplicities that will discourage rebound that occurs in the pure doublet state. The percentage of reactive trajectories leading to the separated radical pair is 98−100% on high-spin (quartet/sextet) energy surfaces, which is significantly higher than that on the doublet energy surface. In Ess and Joy's study, the quintet spin state was found to be the most energetically favorable for the transition states and intermediates with non-heme complexes 1−3, whereas complex 4 favored a doublet spin state. Our work and the work of Ess and Joy are complementary and together provide a complete story of dynamics of both heme and non-heme catalytic oxidations.

■ CONCLUSIONS

DFT calculations and quasi-classical molecular dynamics simulations have been carried out to study the iron porphyrin-catalyzed hydroxylation of ethylbenzene. In the DFT mechanistic study, we found that the H-atom abstraction from ethylbenzene by the iron-oxo species is the rate-determining step. There is a significant barrier for the oxygen rebound step on the high-spin state energy surface, but it is virtually barrierless on the low-spin state energy surface.

In the MD simulations, we found that the HAA transition structure leads to the oxygen rebound and the radical pair separation pathways even on the low-spin doublet surface. The percentage of the oxygen rebound trajectories via ^{2}TS1 is higher than that via ^{4}TS1 and ^{6}TS1. In the hydroxylation of ethylbenzene, the low-spin state reactivity prevails and is characterized by both concerted and stepwise dynamics. The time interval between C−H bond cleavage and C−O bond formation spans from 41 to 619 fs. Conversely, high-spin state catalysis is an energetically stepwise process with a minimal contribution to the production of hydroxylation products. In the gas phase study on ^{2}TS1, 45% of the reactive trajectories lead to the hydroxylated product, and 55% of the reactive trajectories lead to the separated radical pair. In the implicit solvent model study, the percentage of the reactive trajectories leading to the hydroxylation product increases to 56%. The percentage of radical pair separation trajectories in the doublet state was overestimated due to the significant spin contamination present, which favors dissociation. In the radical pair separation trajectories, a few trajectories leading to the styrene or hydroxylation products with inverted configuration can be observed. In addition, the solvent can increase the average time gap of the oxygen rebound pathway.

In conclusion, the iron-porphyrin-catalyzed hydroxylation reaction of ethylbenzene on the doublet energy surface is more

favorable than that on quartet and sextet energy surfaces. The MD simulation results suggest that the reaction on the doublet energy surface is both concerted and stepwise dynamically and can lead to separated radicals. The time gap between C−H bond cleavage and C−O bond formation ranges from 41 to 619 fs. By contrast, the high-spin state catalysis is an energetically stepwise process, and the reaction pathways via high-spin energy surfaces have a negligible contribution to the formation of the hydroxylation product.

■ ASSOCIATED CONTENT

ⓢ Supporting Information

The Supporting Information is available free of charge at https://pubs.acs.org/doi/10.1021/jacs.3c03773.

> Spin densities, orbital diagrams, thresholds for bond formations and trajectory terminations, free energy diagrams of the iron porphyrin-catalyzed C−H hydroxylation, computed energetics of β-hydrogen abstraction, transition state normal mode sampling, dynamics results, distribution of the reactive trajectories, representative trajectories, quantitative distribution, $\langle S_2 \rangle$ values, and Cartesian coordinates of all structures and energies investigated in this work (PDF)
> Inverted configuration trajectory (MP4)
> β-hydrogen abstraction trajectory (MP4)

■ AUTHOR INFORMATION

Corresponding Authors

Yun-Fang Yang − *College of Chemical Engineering, Zhejiang University of Technology, Hangzhou, Zhejiang 310014, China;* ⓞ orcid.org/0000-0002-6287-1640;
Email: yangyf@zjut.edu.cn

K. N. Houk − *Department of Chemistry and Biochemistry, University of California, Los Angeles, California 90095, United States;* ⓞ orcid.org/0000-0002-8387-5261;
Email: houk@chem.ucla.edu

Authors

Yaling Zhang − *College of Chemical Engineering, Zhejiang University of Technology, Hangzhou, Zhejiang 310014, China*

Chaoqin Cao − *College of Chemical Engineering, Zhejiang University of Technology, Hangzhou, Zhejiang 310014, China*

Yuanbin She − *College of Chemical Engineering, Zhejiang University of Technology, Hangzhou, Zhejiang 310014, China;* ⓞ orcid.org/0000-0002-1007-1852

Complete contact information is available at:
https://pubs.acs.org/10.1021/jacs.3c03773

Notes

The authors declare no competing financial interest.

■ ACKNOWLEDGMENTS

■ REFERENCES

(1) (a) Jiao, K. J.; Xing, Y. K.; Yang, Q. L.; Qiu, H.; Mei, T. S. Site-Selective C-H Functionalization via Synergistic Use of Electrochemistry and Transition Metal Catalysis. *Acc. Chem. Res.* **2020**, *53*, 300−310. (b) Yang, Y. F.; Chen, G.; Hong, X.; Yu, J. Q.; Houk, K. N. The Origins of Dramatic Differences in Five-Membered vs Six-Membered Chelation of Pd(II) on Efficiency of C(sp(3))-H Bond Activation. *J. Am. Chem. Soc.* **2017**, *139*, 8514−8521. (c) Chu, L.; Shang, M.; Tanaka, K.; Chen, Q.; Pissarnitski, N.; Streckfuss, E.; Yu, J. Q. Remote Meta-C-H Activation Using a Pyridine-Based Template: Achieving Site-Selectivity via the Recognition of Distance and Geometry. *ACS Cent. Sci.* **2015**, *1*, 394−399.

(2) (a) Ortiz de Montellano, P. R. Hydrocarbon Hydroxylation by Cytochrome P450 Enzymes. *Chem. Rev.* **2010**, *110*, 932−948. (b) Sono, M.; Roach, M. P.; Coulter, E. D.; Dawson, J. H. Heme-Containing Oxygenases. *Chem. Rev.* **1996**, *96*, 2841−2888.

(3) (a) Groves, J. T. Key elements of the chemistry of cytochrome P-450: The oxygen rebound mechanism. *J. Chem. Educ.* **1985**, *62*, 928−931. (b) Groves, J. T.; Adhyam, D. V. Hydroxylation by cytochrome P-450 and metalloporphyrin models. Evidence for allylic rearrangement. *J. Am. Chem. Soc.* **1984**, *106*, 2177−2181. (c) Groves, J. T.; McClusky, G. A. Aliphatic hydroxylation via oxygen rebound. Oxygen transfer catalyzed by iron. *J. Am. Chem. Soc.* **1976**, *98*, 859−861. (d) Groves, J. T.; Van der Puy, M. Stereospecific aliphatic hydroxylation by iron-hydrogen peroxide. Evidence for a stepwise process. *J. Am. Chem. Soc.* **1976**, *98*, 5290−5297.

(4) McMahon, R. E.; Sullivan, H. R.; Craig, J. C.; Pereira, W. E., Jr. The microsomal oxygenation of ethyl benzene: Isotopic, stereochemical, and induction studies. *Arch. Biochem. Biophys.* **1969**, *132*, 575−577.

(5) Newcomb, M.; Shen, R.; Choi, S.-Y.; Toy, P. H.; Hollenberg, P. F.; Vaz, A. D. N.; Coon, M. J. Cytochrome P450-Catalyzed Hydroxylation of Mechanistic Probes that Distinguish between Radicals and Cations. Evidence for Cationic but Not for Radical Intermediates. *J. Am. Chem. Soc.* **2000**, *122*, 2677−2686.

(6) White, R. E.; Miller, J. P.; Favreau, L. V.; Bhattacharyya, A. Stereochemical dynamics of aliphatic hydroxylation by cytochrome P-450. *J. Am. Chem. Soc.* **1986**, *108*, 6024−6031.

(7) Groves, J. T.; McClusky, G. A.; White, R. E.; Coon, M. J. Aliphatic hydroxylation by highly purified liver microsomal cytochrome P-450. Evidence for a carbon radical intermediate. *Biochem. Biophys. Res. Commun.* **1978**, *81*, 154−160.

(8) Liu, W.; Cheng, M.-J.; Nielsen, R. J.; Goddard, W. A., III; Groves, J. T. Probing the C−O Bond-Formation Step in Metalloporphyrin-Catalyzed C−H Oxygenation Reactions. *ACS Catal.* **2017**, *7*, 4182−4188.

(9) Kumar, D.; de Visser, S. P.; Sharma, P. K.; Cohen, S.; Shaik, S. Radical Clock Substrates, Their C−H Hydroxylation Mechanism by Cytochrome P450, and Other Reactivity Patterns: What Does Theory Reveal about the Clocks' Behavior? *J. Am. Chem. Soc.* **2004**, *126*, 1907−1920.

(10) Ogliaro, F.; Harris, N.; Cohen, S.; Filatov, M.; de Visser, S. P.; Shaik, S. A Model "Rebound" Mechanism of Hydroxylation by Cytochrome P450: Stepwise and Effectively Concerted Pathways, and Their Reactivity Patterns. *J. Am. Chem. Soc.* **2000**, *122*, 8977−8989.

(11) (a) Yoshizawa, K.; Kamachi, T.; Shiota, Y. A Theoretical Study of the Dynamic Behavior of Alkane Hydroxylation by a Compound I Model of Cytochrome P450. *J. Am. Chem. Soc.* **2001**, *123*, 9806−9816. (b) Yoshizawa, K.; Shiota, Y.; Kagawa, Y.; Yamabe, T. Femtosecond Dynamics of the Methane−Methanol and Benzene−Phenol Conversions by an Iron−Oxo Species. *J. Phys. Chem. A* **2000**, *104*, 2552−2561.

(12) Sarkar, M. R.; Houston, S. D.; Savage, G. P.; Williams, C. M.; Krenske, E. H.; Bell, S. G.; De Voss, J. J. Rearrangement-Free Hydroxylation of Methylcubanes by a Cytochrome P450: The Case for Dynamical Coupling of C-H Abstraction and Rebound. *J. Am. Chem. Soc.* **2019**, *141*, 19688−19699.

(13) (a) Lan, J.; Li, X.; Yang, Y.; Zhang, X.; Chung, L. W. New Insights and Predictions into Complex Homogeneous Reactions

Enabled by Computational Chemistry in Synergy with Experiments: Isotopes and Mechanisms. *Acc. Chem. Res.* **2022**, *55*, 1109–1123. (b) Yang, Y.; Zhang, X.; Zhong, L. P.; Lan, J.; Li, X.; Li, C. C.; Chung, L. W. Unusual KIE and dynamics effects in the Fe-catalyzed hetero-Diels-Alder reaction of unactivated aldehydes and dienes. *Nat. Commun.* **2020**, *11*, 1850–1859.

(14) Yang, Z.; Yu, P.; Houk, K. N. Molecular Dynamics of Dimethyldioxirane C–H Oxidation. *J. Am. Chem. Soc.* **2016**, *138*, 4237–4242.

(15) (a) Toy, P. H.; Newcomb, M.; Hollenberg, P. F. Hypersensitive Mechanistic Probe Studies of Cytochrome P450-Catalyzed Hydroxylation Reactions. Implications for the Cationic Pathway. *J. Am. Chem. Soc.* **1998**, *120*, 7719–7729. (b) Toy, P. H.; Dhanabalasingam, B.; Newcomb, M.; Hanna, I. H.; Hollenberg, P. F. A Substituted Hypersensitive Radical Probe for Enzyme-Catalyzed Hydroxylations: Synthesis of Racemic and Enantiomerically Enriched Forms and Application in a Cytochrome P450-Catalyzed Oxidation. *J. Org. Chem.* **1997**, *62*, 9114–9122. (c) Newcomb, M.; Le Tadic-Biadatti, M.-H.; Chestney, D. L.; Roberts, E. S.; Hollenberg, P. F. A nonsynchronous concerted mechanism for cytochrome P-450 catalyzed hydroxylation. *J. Am. Chem. Soc.* **1995**, *117*, 12085–12091.

(16) Gelb, M. H.; Heimbrook, D. C.; Malkonen, P.; Sligar, S. G. Stereochemistry and deuterium isotope effects in camphor hydroxylation by the cytochrome P450cam monooxygenase system. *Biochemistry* **1982**, *21*, 370–377.

(17) (a) Ess, D. H. Quasiclassical Direct Dynamics Trajectory Simulations of Organometallic Reactions. *Acc. Chem. Res.* **2021**, *54*, 4410–4422. (b) Maldonado-Domínguez, M.; Srnec, M. Understanding and Predicting Post H-Atom Abstraction Selectivity through Reactive Mode Composition Factor Analysis. *J. Am. Chem. Soc.* **2020**, *142*, 3947–3958. (c) Essafi, S.; Tew, D. P.; Harvey, J. N. The Dynamics of the Reaction of FeO+ and H2: A Model for Inorganic Oxidation. *Angew. Chem., Int. Ed.* **2017**, *56*, 5790–5794.

(18) Joy, J.; Ess, D. H. Direct Dynamics Trajectories Demonstrate Dynamic Matching and Nonstatistical Radical Pair Intermediates during Fe-Oxo-Mediated C–H Functionalization Reactions. *J. Am. Chem. Soc.* **2023**, *145*, 7628–7637.

(19) Frisch, M. J.; Trucks, G. W.; Schlegel, H. B.; Scuseria, G. E.; Robb, M. A.; Cheeseman, J. R.; Scalmani, G.; Barone, V.; Petersson, G. A.; Nakatsuji, H.; Li, X.; Caricato, M.; Marenich, A. V.; Bloino, J.; Janesko, B. G.; Gomperts, R.; Mennucci, B.; Hratchian, H. P.; Ortiz, J. V.; Izmaylov, A. F.; Sonnenberg, J. L.; Williams-Young, D.; Ding, F.; Lipparini, F.; Egidi, F.; Goings, J.; Peng, B.; Petrone, A.; Henderson, T.; Ranasinghe, D.; Zakrzewski, V. G.; Gao, J.; Rega, N.; Zheng, G.; Liang, W.; Hada, M.; Ehara, M.; Toyota, K.; Fukuda, R.; Hasegawa, J.; Ishida, M.; Nakajima, T.; Honda, Y.; Kitao, O.; Nakai, H.; Vreven, T.; Throssell, K.; Montgomery, J. A., Jr.; Peralta, J. E.; Ogliaro, F.; Bearpark, M. J.; Heyd, J. J.; Brothers, E. N.; Kudin, K. N.; Staroverov, V. N.; Keith, T. A.; Kobayashi, R.; Normand, J.; Raghavachari, K.; Rendell, A. P.; Burant, J. C.; Iyengar, S. S.; Tomasi, J.; Cossi, M.; Millam, J. M.; Klene, M.; Adamo, C.; Cammi, R.; Ochterski, J. W.; Martin, R. L.; Morokuma, K.; Farkas, O.; Foresman, J. B.; Fox, D. J. *Gaussian 16, Revision C.01*; Gaussian, Inc.: Wallingford, CT, 2019.

(20) (a) Radoń, M. Spin-State Energetics of Heme-Related Models from DFT and Coupled Cluster Calculations. *J. Chem. Theory Comput.* **2014**, *10*, 2306–2321. (b) Stephens, P. J.; Devlin, F. J.; Chabalowski, C. F.; Frisch, M. J. Ab Initio Calculation of Vibrational Absorption and Circular Dichroism Spectra Using Density Functional Force Fields. *J. Phys. Chem.* **1994**, *98*, 11623–11627. (c) Becke, A. D. A new mixing of Hartree–Fock and local density-functional theories. *J. Chem. Phys.* **1993**, *98*, 1372–1377. (d) Becke, A. D. Density-functional thermochemistry. III. The role of exact exchange. *J. Chem. Phys.* **1993**, *98*, 5648–5652.

(21) (a) Roy, L. E.; Hay, P. J.; Martin, R. L. Revised Basis Sets for the LANL Effective Core Potentials. *J. Chem. Theory Comput.* **2008**, *4*, 1029–1031. (b) Ehlers, A. W.; Böhme, M.; Dapprich, S.; Gobbi, A.; Höllwarth, A.; Jonas, V.; Köhler, K. F.; Stegmann, R.; Veldkamp, A.; Frenking, G. A set of f-polarization functions for pseudo-potential basis sets of the transition metals Sc-Cu, Y-Ag and La-Au. *Chem. Phys.*

Lett. **1993**, *208*, 111–114. (c) Hay, P. J.; Wadt, W. R. Ab initio effective core potentials for molecular calculations. Potentials for K to Au including the outermost core orbitals. *J. Chem. Phys.* **1985**, *82*, 299–310.

(22) (a) Hehre, W. J.; Ditchfield, R.; Pople, J. A. Self—Consistent Molecular Orbital Methods. XII. Further Extensions of Gaussian—Type Basis Sets for Use in Molecular Orbital Studies of Organic Molecules. *J. Chem. Phys.* **1972**, *56*, 2257–2261. (b) Ditchfield, R.; Hehre, W. J.; Pople, J. A. Self-Consistent Molecular-Orbital Methods. IX. An Extended Gaussian-Type Basis for Molecular-Orbital Studies of Organic Molecules. *J. Chem. Phys.* **1971**, *54*, 724–728.

(23) Marenich, A. V.; Cramer, C. J.; Truhlar, D. G. Universal Solvation Model Based on Solute Electron Density and on a Continuum Model of the Solvent Defined by the Bulk Dielectric Constant and Atomic Surface Tensions. *J. Phys. Chem. B* **2009**, *113*, 6378–6396.

(24) Legault, C. Y. *CYLview, 1.0b*; Université de Sherbrooke: Canada, 2009;. http://www.cylview.org (accessed 2021-09-15).

(25) Singleton, D. A.; Wang, Z. Isotope Effects and the Nature of Enantioselectivity in the Shi Epoxidation. The Importance of Asynchronicity. *J. Am. Chem. Soc.* **2005**, *127*, 6679–6685.

(26) Wang, Q.; Chen, X.; Li, G.; Chen, Q.; Yang, Y.-F.; She, Y.-B. Computational Exploration of Chiral Iron Porphyrin-Catalyzed Asymmetric Hydroxylation of Ethylbenzene Where Stereoselectivity Arises from π–π Stacking Interaction. *J. Org. Chem.* **2019**, *84*, 13755–13763.

(27) de Visser, S. P.; Ogliaro, F.; Harris, N.; Shaik, S. Multi-State Epoxidation of Ethene by Cytochrome P450: A Quantum Chemical Study. *J. Am. Chem. Soc.* **2001**, *123*, 3037–3047.

(28) Elenewski, J. E.; Hackett, J. C. Ab initio dynamics of the cytochrome P450 hydroxylation reaction. *J. Chem. Phys.* **2015**, *142*, No. 064307.

(29) (a) Barry, J. T.; Berg, D. J.; Tyler, D. R. Radical Cage Effects: The Prediction of Radical Cage Pair Recombination Efficiencies Using Microviscosity Across a Range of Solvent Types. *J. Am. Chem. Soc.* **2017**, *139*, 14399–14405. (b) Barry, J. T.; Berg, D. J.; Tyler, D. R. Radical Cage Effects: Comparison of Solvent Bulk Viscosity and Microviscosity in Predicting the Recombination Efficiencies of Radical Cage Pairs. *J. Am. Chem. Soc.* **2016**, *138*, 9389–9392. (c) Rabinowitch, E. Collision, co-ordination, diffusion and reaction velocity in condensed systems. *Trans. Faraday Soc.* **1937**, *33*, 1225–1233. (d) Rabinowitch, E.; Wood, W. C. The collison mechanism and the primary photochemical process in solutions. *Trans. Faraday Soc.* **1936**, *32*, 1381–1387. (e) Franck, J.; Rabinowitsch, E. Some remarks about free radicals and the photochemistry of solutions. *Trans. Faraday Soc.* **1934**, *30*, 120–130.

(30) (a) Patel, A.; Chen, Z.; Yang, Z.; Gutierrez, O.; Liu, H. W.; Houk, K. N.; Singleton, D. A. Dynamically Complex [6+4] and [4+2] Cycloadditions in the Biosynthesis of Spinosyn A. *J. Am. Chem. Soc.* **2016**, *138*, 3631–3634. (b) Hong, X.; Bercovici, D. A.; Yang, Z.; Al-Bataineh, N.; Srinivasan, R.; Dhakal, R. C.; Houk, K. N.; Brewer, M. Mechanism and Dynamics of Intramolecular C–H Insertion Reactions of 1-Aza-2-azoniaallene Salts. *J. Am. Chem. Soc.* **2015**, *137*, 9100–9107. (c) Yang, Z.; Doubleday, C.; Houk, K. N. QM/MM Protocol for Direct Molecular Dynamics of Chemical Reactions in Solution: The Water-Accelerated Diels-Alder Reaction. *J. Chem. Theory Comput.* **2015**, *11*, 5606–5612. (d) Black, K.; Liu, P.; Xu, L.; Doubleday, C.; Houk, K. N. Dynamics, transition states, and timing of bond formation in Diels-Alder reactions. *Proc. Natl. Acad. Sci. U. S. A.* **2012**, *109*, 12860–12865. (e) Xu, L.; Doubleday, C. E.; Houk, K. N. Dynamics of carbene cycloadditions. *J. Am. Chem. Soc.* **2011**, *133*, 17848–17854.

(31) (a) Ma, L.; Koka, J.; Stace, A. J.; Cox, H. Gas Phase UV Spectrum of a Cu(II)—Bis(benzene) Sandwich Complex: Experiment and Theory. *J. Phys. Chem. A* **2014**, *118*, 10730–10737. (b) Swart, M.; Güell, M.; Luis, J. M.; Solà, M. Spin-State-Corrected Gaussian-Type Orbital Basis Sets. *J. Phys. Chem. A* **2010**, *114*, 7191–7197. (c) Menon, A. S.; Radom, L. Consequences of Spin Contamination in Unrestricted Calculations on Open-Shell Species: Effect of Hartree—

Fock and Møller−Plesset Contributions in Hybrid and Double-Hybrid Density Functional Theory Approaches. *J. Phys. Chem. A* **2008**, *112*, 13225−13230. (d) Chuang, Y.-Y.; Coitiño, E. L.; Truhlar, D. G. How Should We Calculate Transition State Geometries for Radical Reactions? The Effect of Spin Contamination on the Prediction of Geometries for Open-Shell Saddle Points. *J. Phys. Chem. A* **2000**, *104*, 446−450. (e) Chen, W.; Schlegel, H. B. Evaluation of S2 for correlated wave functions and spin projection of unrestricted Mo/ller−Plesset perturbation theory. *J. Chem. Phys.* **1994**, *101*, 5957−5968. (f) Schlegel, H. B. Moeller-Plesset perturbation theory with spin projection. *J. Phys. Chem.* **1988**, *92*, 3075−3078. (g) Schlegel, H. B. Potential energy curves using unrestricted Mo/ller−Plesset perturbation theory with spin annihilation. *J. Chem. Phys.* **1986**, *84*, 4530−4534.

(32) (a) Zhang, R.; Yu, W.-Y.; Lai, T.-S.; Che, C.-M. Enantioselective hydroxylation of benzylic C−H bonds by D4-symmetric chiral oxoruthenium porphyrins†. *Chem. Commun.* **1999**, 1791−1792. (b) Groves, J. T.; Viski, P. Asymmetric hydroxylation by a chiral iron porphyrin. *J. Am. Chem. Soc.* **1989**, *111*, 8537−8538.

(33) (a) Li, R.-J.; Tian, K.; Li, X.; Gaikaiwari, A. R.; Li, Z. Engineering P450 Monooxygenases for Highly Regioselective and Active p-Hydroxylation of m-Alkylphenols. *ACS Catal.* **2022**, *12*, 5939−5948. (b) Grobe, S.; Badenhorst, C. P. S.; Bayer, T.; Hamnevik, E.; Wu, S.; Grathwol, C. W.; Link, A.; Koban, S.; Brundiek, H.; Grossjohann, B.; Bornscheuer, U. T. Engineering Regioselectivity of a P450 Monooxygenase Enables the Synthesis of Ursodeoxycholic Acid via 7beta-Hydroxylation of Lithocholic Acid. *Angew. Chem., Int. Ed.* **2021**, *60*, 753−757. (c) Li, R.-J.; Li, A.; Zhao, J.; Chen, Q.; Li, N.; Yu, H.-L.; Xu, J.-H. Engineering P450LaMO stereospecificity and product selectivity for selective C−H oxidation of tetralin-like alkylbenzenes. *Catal. Sci. Technol.* **2018**, *8*, 4638−4644. (d) Pham, S. Q.; Pompidor, G.; Liu, J.; Li, X.-D.; Li, Z. Evolving P450pyr hydroxylase for highly enantioselective hydroxylation at non-activated carbon atom. *Chem. Commun.* **2012**, *48*, 4618−4620. (e) Kille, S.; Zilly, F. E.; Acevedo, J. P.; Reetz, M. T. Regio- and stereoselectivity of P450-catalysed hydroxylation of steroids controlled by laboratory evolution. *Nat. Chem.* **2011**, *3*, 738−743.

(34) (a) Chen, Z.; Nieves-Quinones, Y.; Waas, J. R.; Singleton, D. A. Isotope Effects, Dynamic Matching, and Solvent Dynamics in a Wittig Reaction. Betaines as Bypassed Intermediates. *J. Am. Chem. Soc.* **2014**, *136*, 13122−13125. (b) Glowacki, D. R.; Orr-Ewing, A. J.; Harvey, J. N. Product energy deposition of CN + alkane H abstraction reactions in gas and solution phases. *J. Chem. Phys.* **2011**, *134*, 214508. (c) Sato, M.; Yamataka, H.; Komeiji, Y.; Mochizuki, Y.; Ishikawa, T.; Nakano, T. How Does an S_N2 Reaction Take Place in Solution? Full Ab Initio MD Simulations for the Hydrolysis of the Methyl Diazonium Ion. *J. Am. Chem. Soc.* **2008**, *130*, 2396−2397. (d) Ruiz-Pernía, J. J.; Tuñón, I.; Moliner, V.; Hynes, J. T.; Roca, M. Dynamic Effects on Reaction Rates in a Michael Addition Catalyzed by Chalcone Isomerase. Beyond the Frozen Environment Approach. *J. Am. Chem. Soc.* **2008**, *130*, 7477−7488. (e) Acevedo, O.; Jorgensen, W. L. Understanding Rate Accelerations for Diels−Alder Reactions in Solution Using Enhanced QM/MM Methodology. *J. Chem. Theory Comput.* **2007**, *3*, 1412−1419. (f) Chandrasekhar, J.; Shariffskul, S.; Jorgensen, W. L. QM/MM Simulations for Diels−Alder Reactions in Water: Contribution of Enhanced Hydrogen Bonding at the Transition State to the Solvent Effect. *J. Phys. Chem. B* **2002**, *106*, 8078−8085. (g) Mann, D. J.; Halls, M. D. Ring-opening of the cyclopropyl radical in the condensed phase: A combined density functional theory/molecular mechanics quasiclassical trajectory study. *Phys. Chem. Chem. Phys.* **2002**, *4*, 5066−5071. (h) Rideout, D. C.; Breslow, R. Hydrophobic acceleration of Diels-Alder reactions. *J. Am. Chem. Soc.* **1980**, *102*, 7816−7817.